Classification and Location of Cerebral Hemorrhage Points Based on SEM and SSA-GA-BP Neural Network

Qinwei Li, *Member, IEEE*, Lunxiao Wang, Xiaoguang Lu, *Member, IEEE*, Dequan Ding, Yang Zhao, *Member, IEEE*, Jianwei Wang, *Member, IEEE*, Xinze Li, Hang Wu, Guang Zhang, Ming Yu, and Ping Han

***Abstract*— In this article, a method to fast classify (intradural hemorrhage, epidural hemorrhage, and cerebral parenchymal hemorrhage) and locate the bleeding points by using the singularity expansion method (SEM) and backpropagation (BP) neural network optimized by genetic algorithm (GA) and sparrow search algorithm (SSA) is proposed. In the simulation model, the bleeding spot with a radius of 3 mm is successfully identified by the approach. The test accuracy in the simulation for both the bleeding's localization and classification are 98.0% and 97.4%, respectively. Head phantoms that have all been improved over the previous phantom established are used for experiments. A bleeding target with a volume of 3 mL can be identified in the microwave detection system. In the experiment, the accuracy of classification and localization of the bleeding type are 90% and 94.7%, respectively. The final results demonstrate the capability and effectiveness of the method. Faster determination of bleeding point type and orientation means that patients can be provided with different rescue measures accordingly.**

***Index Terms*— Classification of cerebral hemorrhage, localization of cerebral hemorrhage, microwave signal, singularity expansion method (SEM), sparrow search algorithm-genetic algorithm-back propagation (SSA-GA-BP) neural network.**

I. Introduction

STROKE has become one of the diseases with extremely high mortality. On average, one in four people over the age of 25 in the world may have a stroke. The longer it takes, the more blood you will bleed. The golden rescue time for a stroke is 4–5 h, the earlier treatment means less harm to the patient [1]. Therefore, to save more patients' lives, the time for early diagnosis and treatment of stroke is very precious. At present, the general medical instruments used to detect the bleeding point of stroke are computed tomography (CT) detectors and magnetic resonance imaging (MRI) detectors [2]. However, these two instruments are complex to use and bulky, and they are not portable medical devices, so they are not convenient for outdoor rescue and other special scenes.

Microwave tomography (MWT) is a new imaging technique, which has been applied to the early diagnosis of breast cancer [3]. At present, a novel stroke detection system using microwave imaging technology is being gradually deepened by various research groups. One of the advantages of microwave monitoring is equipment volume. Besides, the detection cost is low, and the detection speed is fast. So, the microwave detection system is expected to become a new generation of equipment to detect strokes for public [4], [5]. MWT technology is a kind of non-destructive testing. In the early stage, different dielectric properties of various brain tissues responding to microwave signals can be used to reconstruct the real brain structure. Therefore, brain structures without abnormalities and those with hemorrhagic spots can also be distinguished due to their different electromagnetic properties [6].

There are now several research groups dedicated to early stroke detection and identification system research, in general, most of the research is looking for bleeding point targets in simple phantoms and imaging-detected targets [7], [8], [9]. Some methods are time-consuming using inverse scattering. The inversion method among these methods can correctly evaluate the performance of the reconstruction model method. But the iterative time cost is fatal [2], [10], [11]. Rodriguez-Duarte et al.'s [12], [13] team at the Polytechnic University of Turin has been working on microwave stroke classification detection. They proposed a method by using differential approximations and distorted Born approximations to image the target [12], [13]. Mariano et al.'s [14] team at the Polytechnic University of Turin used a dataset generated by full-wave simulation to test the type and direction of stroke. The group of King's College London, Strand, London, applied the distorted Born iterative method, two-step iterative shrinkage thresholding

Manuscript received 8 November 2023; revised 11 December 2023; accepted 12 December 2023. Date of publication 1 January 2024; date of current version 15 January 2024. This work was supported by "The Fundamental Research Funds for the Central Universities" funded by the Civil Aviation University of China under Grant 3122023021. The Associate Editor coordinating the review process was Dr. Gabriele Patrizi. *(Corresponding author: Ming Yu.)*

Qinwei Li, Lunxiao Wang, Xiaoguang Lu, Dequan Ding, Yang Zhao, Jianwei Wang, and Ping Han are with the Tianjin Key Laboratory for Advanced Signal Processing, Civil Aviation University of China, Tianjin 300300, China (e-mail: qw_li@cauc.edu.cn; wlx1076259534@163.com; xglu@cauc.edu.cn; ddq0124@163.com; zhaoy@cauc.edu.cn; wangjianwei18863@163.com; phan@cauc.edu.cn).

Xinze Li is with Yingkou Jucheng Teaching Technology Development Company Ltd., Huludao, Liaoning 115000, China (e-mail: jucheng1181@163.com).

Hang Wu, Guang Zhang, and Ming Yu are with the Medical Support Technology Research Department, Systems Engineering Institute, Academy of Military Science, Tianjin 300161, China (e-mail: 2008.wuhang@163.com; zg-crazy@163.com; yuming_1990@outlook.com).

Digital Object Identifier 10.1109/TIM.2023.3348908

(DBIM-TwIST) algorithm to differentiate the hemorrhagic and ischemic strokes [15], [16], [17]. In the latest study, the team from Czech Technical University used support vector machines (SVMs) to establish a comprehensive training set, which can classify hemorrhagic stroke and ischemic stroke [18]. The head phantom used in this reference only contains one material with dielectric properties equal to the average dielectric parameters of a human head. In this article, the raw signals were set as the input data of the learning-by-example (LBE) strategies. The study in [18] is a continuation of the previous research in [19]. In [18], the raw signals were proposed by using the principal component analysis (PCA) algorithm to improve the accuracy of the classification. However, the algorithms proposed in [19] only trained on the data obtained from numerical simulations. The above research teams have made a great breakthrough in the research on the imaging part of the stroke. Stroke rescue detection needs the necessary conditions of urgency and speediness. Qualitative analysis of the bleeding type and bleeding location is in the first place. Analyzing the bleeding type first and then determining the location can narrow the imaging range, which is the necessary prerequisite for small-scale and high-efficiency imaging in detection. Determining the type and the orientation of the bleeding point is also very important for early rescue and protection of patients.

To solve the above problems, this article proposed a method using singularity expansion method (SEM) and sparrow search algorithm-genetic algorithm-backpropagation (SSA-GA-BP) neural networks to quickly classify and locate the types of bleeding points. In this study, only the time-domain signal is needed to extract the feature singularity as the input data of the neural network. The attenuation factor and amplitude at the corresponding frequency are extracted from the time-domain signal. Classification efficiency can be significantly increased by using fewer features and fewer classification labels. This method combines the signal processing method and the neural network to identify the cerebral hemorrhage, which saves a lot of detection time. Table I provides a side-by-side comparison between the work presented in this article and the most recent related research.

The details of the research in this article are described as follows. In Section II, the details of establishing the 2-D head model by applying the finite-difference time domain (FDTD) method are shown. The details of the proposed method used in the simulation will be shown in Section III. The results of the simulation and discussions are shown in Section IV. Section V shows the experiment verification of the proposed method. The conclusion of this article is presented in Section VI.

II. Head Modeling in Simulation

In this section, the details of the 2-D model of the brain in the simulation and the electromagnetic characteristics of brain tissues will be shown. The details of the antenna set around the head model will also be introduced in this section.

A. Electromagnetic Characteristics of the Brain Tissue

The structure of the human brain is complicated. Fig. 1 is an MRI of the real head, which shows the main structure of the human head. This MRI of the head is the key data for simulation modeling. It can be seen in Fig. 1 that the scalp is the outermost layer of the head, which is together with subcutaneous fat to protect the head. The skull plays a supporting and protecting role. Further inside are meningeal structures, including cerebrospinal fluid, and fat tissues between the skull and the brain. Deep inside the brain are the gray matter and white matter. In Fig. 1, the chosen main structures in the simulation modeling are labeled.

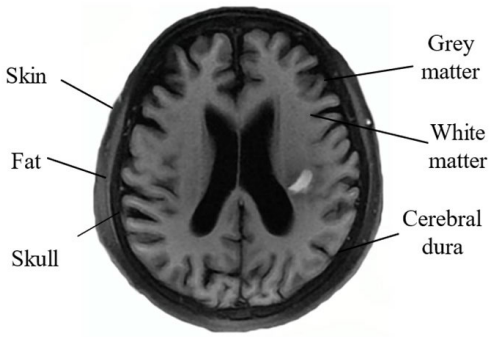

Fig. 1. MRI of the human brain.

The electromagnetic characteristics of human brain tissue are the basis of analyzing the propagation of microwave signals in the brain. Human tissues have different electrical properties [20]. Human biological tissues show different reaction effects in the external electromagnetic field due to their different electrical characteristics. Electrical characteristics include conductive characteristics and dielectric characteristics [21].

FDTD iterative analysis is applied in this study. The ideal frequency band is selected within 1–5 GHz according to relevant research results [22]. The electromagnetic parameters of the brain tissue at 1 GHz are shown in Table II.

B. FDTD Simulation of Head Model

The head modeling in this article is based on the 2-D FDTD method. Before the iterative operation of FDTD, the analysis and processing of the MRI are carried out. The MRI is separated and labeled for each brain tissue so that the electromagnetic parameters can be assigned to each computing cell in the subsequent iterative operation [16], [23], [24]. Fig. 2 shows the established 2-D head model and the location of the antenna array. Each color represents a tissue. The portion outside the head in the figure is set as an air layer.

To simulate the antenna position of the stroke detection equipment, the 16 antennas are evenly arranged around the scalp. During the detection, one antenna transmits a signal, the other antennas receive the signal, respectively. In this simulation, the emitted signal is set as the sixth-order Gaussian pulse signal [25].

III. Signal Data Processing and Classification

In this section, the approach of signal processing is specified. Different bleeding point types and orientations are set as

TABLE I
RESEARCH METHODS AND RESULTS OF THE ABOVE TEAMS

Reference	Results	Novelty	Limitations
[7]	Determine whether the bleeding site is an ischemic or hemorrhagic stroke. The imaging target size of $10mm^3$ to $35mm^3$ volume.	Graph degree mutual information approach.	Need to progress with actual experiments.
[8]	9 representative locations of intradural and epidural hemorrhage were discriminated and imaged in the experiment.	Gauss-Newton Algorithm with Tikhonov regularization.	Low sensitivity, spatial resolution, and sensitivity to noise.
[9]	Simulation to validate the physiological evolution of ischemic stroke from attack to chronic state.	EMT technology and the second generation of EMT brain scanner.	Need matching medium. High computational cost.
[10]	Simulations were imaged stroke models with radii of 1.5 cm and 2.5 cm. Experiments were imaged stroke models with radii of 3 cm, 1 cm, and 0.5 cm.	An image reconstruction algorithm based on the Lebesgue space inversion method.	Need more comprehensive validation of the system.
[11],[2]	Cylinders filled with simulated liquids were used to model the brain and the bleeding point in both experiments and simulations.	A variable-exponent Lebesgue-space regularization technique.	Need of a priori information for improving results.
[12],[13]	The system images ischemic and hemorrhagic strokes that vary in size around 1 cm.	Differential approximations and distorted Born approximations and the brick-shaped antenna module.	Need to progress with actual experiments.
[14]	Identify the presence or absence of the stroke, the kind of stroke (hemorrhagic or ischemic), and its position within the brain.	A dataset generated by full-wave simulation and machine learning algorithms trained with a linearized scattering operator.	Need to progress with actual experiments.
[15],[16], [17]	Discriminate between ischemic and hemorrhagic stroke and imaged. The effect of the presence or absence of metamaterials on the effectiveness was compared.	The distorted Born iterative method, two-step iterative shrinkage thresholding (DBIM-TwIST) algorithm. Incorporation of metamaterials in experimental antennas.	The experimental phantom in this study is oversimplified.
[18]	The presence of stroke was detected and classified (ischemic or hemorrhagic). The classification accuracy was 95.8%.	Principal component analysis (PCA) through singular value decomposition (SVD).	Need to find suitable training data to accurately detect and classify the type of stroke located at an arbitrary position in the head.
[19]	The presence of stroke was detected and classified (ischemic or hemorrhagic).	Learning-by-Examples.	This "end-to-end" mode requires more verification of stability.
This paper	In the experiment, the cerebral hemorrhage with a volume of 3 ml can be located and classified successfully.20 seconds are taken for the processing procedure.	Singularity Expansion Method (SEM) and Backpropagation (BP) neural network optimized by genetic algorithm (GA) and Sparrow Search Algorithm (SSA)	Need more sizes of the hemorrhage point and more situations of a head phantom.

TABLE II
ELECTROMAGNETIC PARAMETERS OF BRAIN TISSUES

Brain tissue	Relative Dielectric Constant	Conductivity *(S/m)*
Skin	40.95	0.089
Fat	5.45	0.052
Skull	12.03	0.202
Cerebral dura	68.02	2.506
Grey matter	52.282	0.985
White matter	46.00	0.82
Blood	61.00	1.600

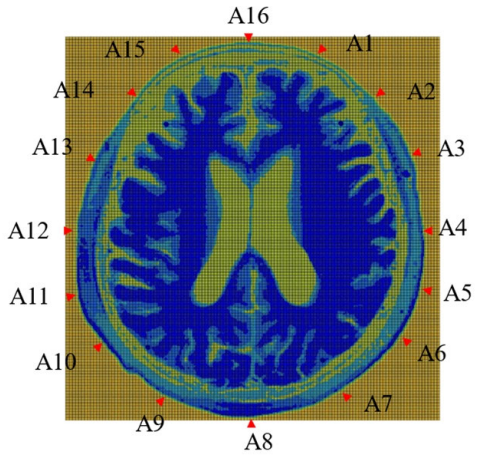

Fig. 2. Simulation model of the head and the location of the antennas.

different category labels for the collected raw signals. Then, the unique feature singularity information is extracted from the original signals. Finally, the GA-BP neural network is used in the simulation stage to classify the location and type of bleeding points. In the experimental detection phase, the SSA-GA-BP neural network is used to classify the location and type of bleeding targets.

A. Set Category Label

In this section, a bleeding spot with a radius of 3 mm is set in the brain model. Three bleeding types and four orientations of the bleeding target are used as the labels of the received raw signals. In the simulation, each type of bleeding target has four orientations. Fig. 3(a) shows the epidural hemorrhage, which is one of the most common types of hemorrhage in reality. Also, four positions (top left, top right, bottom left, and bottom right) of the epidural hemorrhages are shown in Fig. 3(a). In Fig. 3(b), the intradural hemorrhages with four

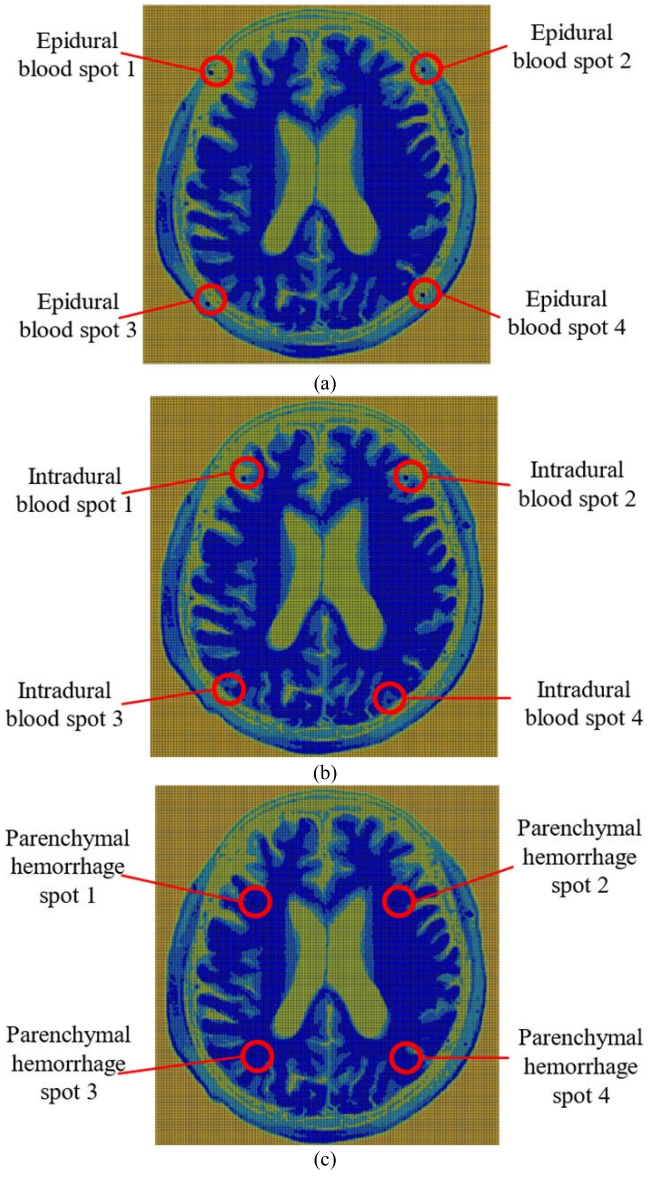

Fig. 3. Three different types of bleeding points with a radius of 3 mm are set in the 2-D model. (a) Epidural hemorrhage model with bleeding points in four directions. (b) Intradural hemorrhage model with bleeding points in four directions. (c) Parenchymal hemorrhage model with bleeding points in four directions.

orientations are shown, and in Fig. 3(c), the parenchymal hemorrhages with four orientations are shown. The raw signals obtained from these 12 simulation models are first labeled by the three bleeding types. Then, four orientations were used as the second labels to distinguish the signals obtained from different locations of cerebral hemorrhage.

The central coordinate position of each bleeding point will be shown in Table III. In this article, each orientation of a particular kind of bleeding point is set as a label, so there are 12 different types of labels in total. After determining the tag, the FDTD method is applied to obtain the raw signals. During the detection, one antenna transmits a signal, the other antennas receive the signal, respectively. A 16×15 signal matrix is obtained after a single detection.

TABLE III
FEATURE POLES INFORMATION OF DIFFERENT TYPES AND DIFFERENT LOCATIONS OF BLEEDING POINTS

Hemorrhagic spot type	Center coordinates	A_m	$\alpha_m(N_p/s)$	f_m(GHz)
Epidural hemorrhage	(184,438)	6.7739e-11	3.1476e+08	1.2276e+09
	(461,442)	2.3010e-11	3.6477e+08	1.0697e+09
	(180,130)	1.4038e-11	3.6480e+08	1.0697e+09
	(460,142)	1.4699e-11	3.6473e+08	1.0697e+09
Intradural hemorrhage	(220,421)	1.6421e-11	4.0255e+08	7.7443e+08
	(430,422)	1.3745e-11	3.9071e+08	9.1958e+08
	(198,144)	1.7168e-11	3.1470e+08	1.2276e+09
	(408,128)	8.7658e-10	3.6476e+08	1.0697e+09
Parenchymal hemorrhage	(253,404)	6.5897e-12	3.1472e+08	1.2276e+09
	(397,437)	1.8644e-11	3.9072e+08	9.1958e+08
	(211,179)	1.0194e-11	3.6476e+08	1.0697e+09
	(420,150)	1.1705e-11	3.6475e+08	1.0697e+09

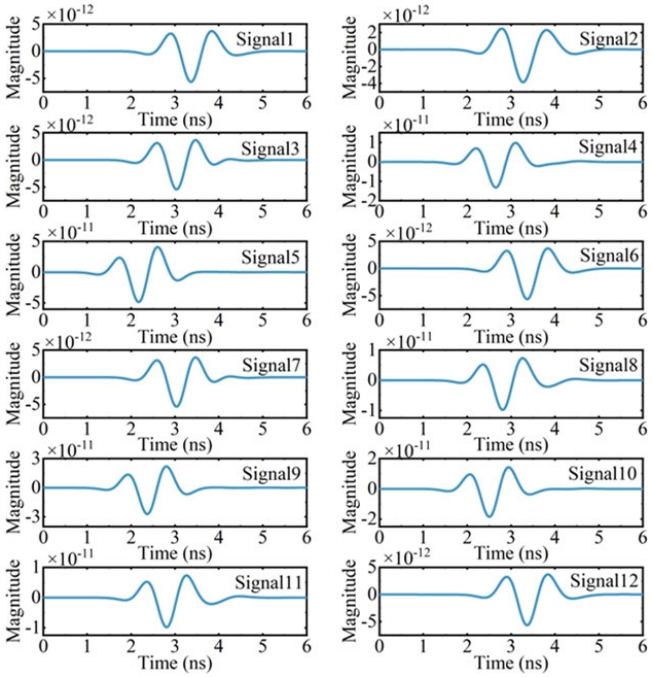

Fig. 4. Signals received by A_8 and emitted by A_1 in 12 bleeding models.

Then, a total of 12signal matrices are obtained. Fig. 4 shows the signals related to different types of bleeding received by the A_8 antenna, when the A_1 antenna emits the signal. Signals 1–4 are the signals of the epidural hemorrhage located at the top left, top right, bottom left, and bottom right. Signals 5–8 are the signals of the intradural hemorrhage located at the top-left, top-right, bottom-left, and bottom-right directions. Signals 9–12 are the signals of the parenchymal hemorrhage located at the top left, top right, bottom left, and bottom right. It can be seen from the figure that the amplitude difference between different signals is not obvious, and it is hard to judge the label category by these raw signals.

B. Extraction of Feature Poles

After obtaining all the raw signals related to different types of bleeding points, the singular point expansion method is applied to the analysis of transient electromagnetic fields due to the natural resonance phenomenon of the electromagnetic system itself [26], [27]. Signal pole extraction is a very important application in radar target recognition, nuclear magnetic resonance, speech recognition, and other fields.

The current model-based linear prediction pole extraction methods mainly include the Prony method, the general pencil of functions (GPOFs), and the matrix pencil method (MPM). In the direction of early breast tumor target recognition, the characteristic poles of the tumor are extracted through the Prony algorithm in the singular point expansion method, so that different growth stages of the tumor can be identified [28], [29], [30]. Finally, this research chooses the Prony algorithm to extract the characteristic poles of the signals.

The Prony algorithm is actually a polynomial calculation method, and its most essential problem is to extract pole information from instantaneous data with equal time intervals. Here, the signal $y(t)$ obtained by FDTD iteration is discretized to obtain $y(n)$. Denote $y(n)$ as a signal model of attenuation exponential sum

$$y(n) = \sum_{m=1}^{p} b_m \cdot z_m^n, \quad n = 0, 1, \ldots, N-1. \tag{1}$$

The pole information is represented by z_m

$$z_m = e^{si \cdot t} = e^{(-\alpha_i + j\omega_i)t}, \quad m = 1, 2, \ldots, M. \tag{2}$$

In order to perform signal analysis, it is necessary to extract the characteristic components from the signal represented by (2), that is, it is necessary to extract the best M. Prony's theoretical definition constructs a sample function matrix R

$$R = \begin{bmatrix} r(0,0) & r(0,1) & \ldots & r(0,pe) \\ r(1,0) & r(1,1) & \ldots & r(1,pe) \\ \vdots & \vdots & \ddots & \vdots \\ r(pe,0) & r(pe,1) & \cdots & r(pe,pe) \end{bmatrix}_{(pe+1)\times(pe+1)}$$

where p is the real order of the Prony algorithm, generally take $P_e = N/2$, and N is the time step of the signal. During FDTD iteration, the iteration time step is set as 6000 steps, so $N = 6000$

$$r(i, j) = \sum_{n=P_e}^{N-1} y(n-j)y^*(n-i). \tag{3}$$

The following uses singular value decomposition (SVD) to determine the effective rank P of the matrix R. The dimension of the matrix $S^{(p)}$ is $(p+1) \times (p+1)$

$$S^{(p)} = \sum_{j=1}^{p} \sum_{i=1}^{P_e - p + 1} \sigma_{jj}^2 v_j^i \left(v_j^i\right)^H \tag{4}$$

where σ_{jj}^2 is singular values of matrix R

$$v_j^i = \left[v(i, j), v(i+1, j), \ldots, v(i+p, j)\right]^T. \tag{5}$$

$v(i, j)$ is a factor on row i and column j of matrix v.

Finally, a and z need to be solved. The relationship between a and z is as follows:

$$1 + a_1 z^{-1} + \cdots + a_p z^{-p} = 0 \tag{6}$$

where a is represented by the following equation:

$$a_i = \frac{S^{(-p)}(i+1, 1)}{S^{(-p)}(1, 1)}, \quad i = 1, \ldots, p. \tag{7}$$

$S^{(-p)}$ is the inverse matrix of $S^{(p)}$. At this time, assuming that z has been obtained, (1) can be simplified to the equation of parameter b in the following equation:

$$\Phi b = y(n)$$
$$\Phi = \begin{bmatrix} 1 & 1 & \ldots & 1 \\ Z_1 & Z_2 & \ldots & Z_1 \\ \vdots & \vdots & \ddots & \vdots \\ Z_1^{N-1} & Z_2^{N-1} & \ldots & Z_P^{N-1} \end{bmatrix}. \tag{8}$$

The relationship between b and Φ is $b = [\Phi^H \Phi]^{-1} \Phi^H \cdot y$. According to b, the information contained in the characteristic singularity can be obtained, including amplitude, attenuation factor, and frequency. The amplitude, attenuation factor, and frequency can be calculated by using the following equation:

$$A_m = |b_k|$$
$$\alpha_m = \frac{ln|z_k|}{\Delta t}$$
$$f_m = \arctan\left[\frac{I_m(z_k)}{R_e(z_k)}\right] / 2\pi\,\Delta t. \tag{9}$$

Then, the corresponding feature pole information, including amplitude, attenuation factor, and frequency of all the signals, can be obtained according to the abovementioned method. Table III shows the feature poles information. Different information corresponds to signals obtained from the simulation model with different bleeding points. The center coordinates are the positions of the bleeding points. They are the coordinates of the center of the bleeding point in the set 2-D model. The bottom-left corner of the 2-D model in Fig. 2 is defined as the coordinate origin. In Table III, only a set of information at 1 GHz corresponding to each signal is shown. There are 2200 sets of pole information obtained in the actual calculation. The data volume is so huge that it cannot be fully displayed here.

C. SSA-GA-BP Neural Network

This section shows the procedure of classifying the feature poles dataset obtained in Section III-B. There are many types of neural networks at present, but in this study, the SSA-GA-BP neural network is selected as the neural network model for classification. BP neural network is the most complete series of artificial neural network methods so far, and it is easier to apply to actual test scenarios [31], [32]. BP neural network is mainly composed of an input layer, hidden layer, and output layer [33].

In this study, two networks are designed. The output layer of the first network has three outputs to help classify the type

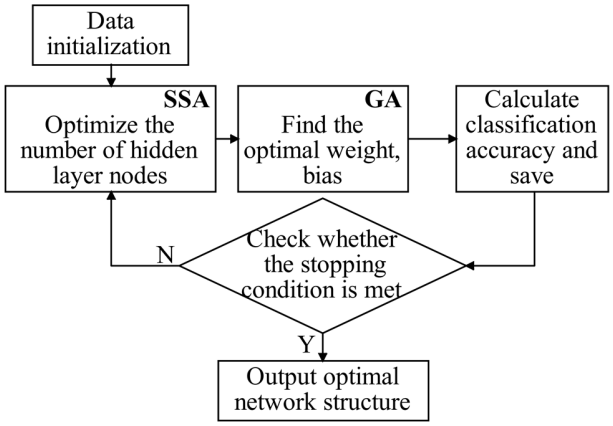

Fig. 5. Flowchart of the optimization algorithm.

of bleeding target. The output layer of the second network has four outputs to help locate the bleeding target.

The overall performance of the BP network particularly depends on the initial weights and bias. So, how to obtain the initial weights and biases correctly is a key issue in improving the performance of the BP neural network [34]. The most suitable weights and biases for the network need to be chosen. The number of hidden layers and the number of nodes in the BP neural network play a decisive role in the training speed and recognition accuracy of the entire network [35]. SSA-GA optimization of the BP neural network can focus on solving these two problems. The SSA intelligence algorithm is a relatively novel swarm intelligence optimization algorithm. The core of the algorithm is inspired by sparrows' strategies of finding food and dealing with natural enemies. Compared with other popular optimization algorithms, the sparrow search algorithm (SSA) improves the search accuracy of the sample target and reduces the optimization time.

The genetic algorithm transforms the selection of initial weight and threshold into the problem of solving the optimal value of the function and assigns it to the BP neural network after selection. In terms of the selection of hidden layers, too many hidden layers and the number of nodes will have a negative impact on the network and negatively damage the processing capacity of the network.

The flowchart of the optimization algorithm is shown in Fig. 5. In the optimization process, the data are initialized first. Then, the SSA algorithm is used to find the appropriate number of hidden layer nodes. GA optimization algorithm optimizes the corresponding weight and bias. Then, the stopping condition is checked to decide whether to continue or to repeat the above loop. The stopping condition is whether the loss function (multiclass cross-entropy) in the network has converged within the set epochs. It will also check whether the current number of SSA iterations is the same as the set number of stops.

It is worth noting that the signal in the simulation stage is obtained under the ideal condition, so its characteristics are more obvious, and the optimal network can be obtained only by GA algorithm optimization in the simulation stage. The number of nodes, the weight, and the bias in the network are

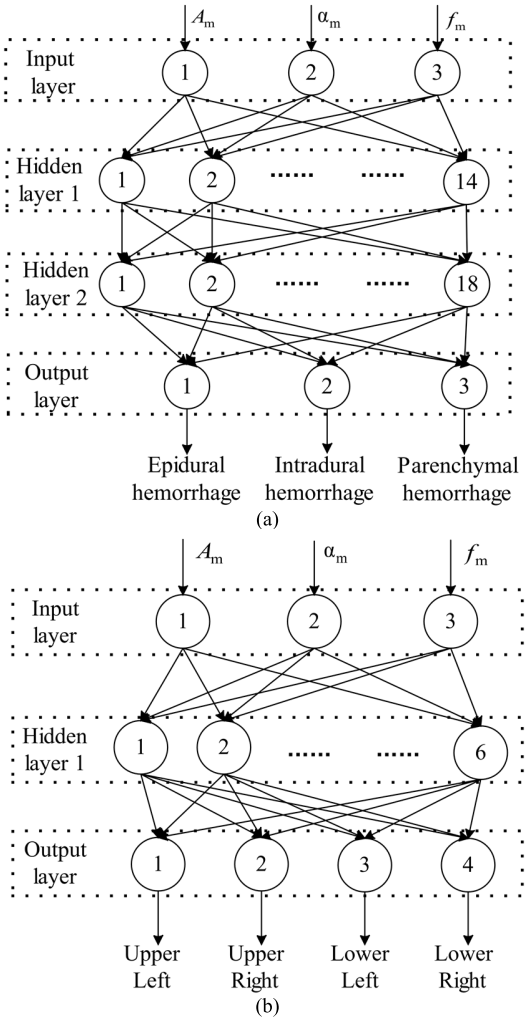

Fig. 6. Final network structure optimized by the genetic algorithm. (a) First neural network for judging the type of bleeding point. (b) Second neural network for judging the direction of the bleeding point.

all the optimization results of the GA algorithm. The number of hidden layers has been verified by multiple tests, and two layers can meet the classification accuracy requirements. One hidden layer can meet the location accuracy requirements in the localization network.

During the simulation, the final network structure optimized by the genetic algorithm is shown in Fig. 6. Fig. 6(a) is the first neural network for judging the type of bleeding point in the simulation phase. The number of nodes in the first hidden layer is 14. The number of nodes in the second hidden layer is 18. The number of nodes in the output layer is 3. Fig. 6(b) is the second neural network for judging the direction of the bleeding point in the simulation phase. This neural network is a single hidden layer neural network with six nodes, the number of nodes in the output layer is 4.

The ultimate research purpose is not only to determine the type of cerebral hemorrhage point but also to determine the location of the hemorrhage point, to facilitate the later imaging processing, or to provide corresponding protection measures for patients. The specific process of the overall detection method is shown in Fig. 7. First, the raw signals are collected

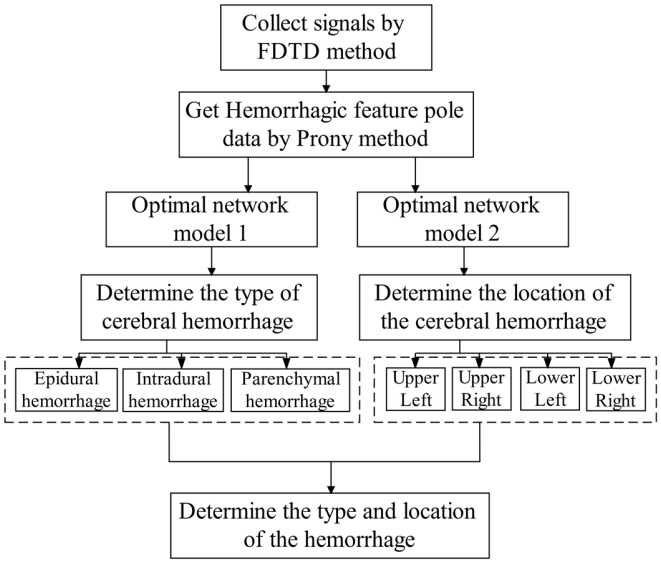

Fig. 7. Specific process of the overall detection method.

from FDTD models. Then, the raw signals are processed by SEM method to achieve the characteristic poles, which are set as the input data of the neural network. The first network classifies the type of cerebral hemorrhage, whereas the second network judges the orientation of cerebral hemorrhage.

IV. Simulation Results and Discussion

This section contains the results and discussions of the proposed method in the simulation model.

The obtained 2200 sets of extreme point information were randomly divided into two groups, one group was used to test the first network for judging the type of bleeding point, and the other group was used to test the second network for judging the direction of bleeding point. Both networks have 1100 feature poles information. To improve the accuracy of judgment, the pole data are cleaned by the data cleaning method, which is also a method for data quality analysis. The data cleaning method is the process of reviewing and verifying data to remove duplicates, correct errors, and provide data consistency. After data cleaning, there are 1037 sets of data input into the first network and 1008 sets of data input into the second network. The data cleaning procedures of the two networks are different because the number of label categories is different. Although the number of cleaned data is different, it does not affect subsequent tests. In this study, 85% of the total data is selected as the training set and 15% as the test set. That is, the first network has 882 sets for training and 155 sets for testing. The second network has 857 sets for training and 151 sets for testing.

Fig. 8 shows the confusion matrix diagram for the bleeding point type classification network. Fig. 8(a) is the training set's confusion matrix diagram, and Fig. 8(b) is the test set's confusion matrix diagram. The abscissa represents the predicted label of the sample, where 1 represents epidural hemorrhage, 2 represents intradural hemorrhage, and 3 represents parenchymal hemorrhage. The ordinate represents the true label of the sample. The accuracy of the training set is 98.9%. The accuracy on the test set is 97.4%.

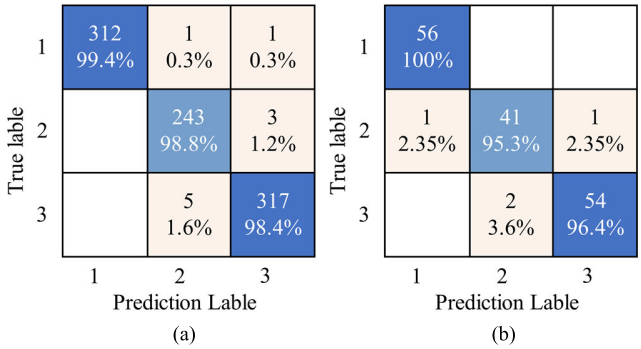

Fig. 8. Confusion matrix diagram of the classification neural network. (a) Training set's confusion matrix diagram. (b) Test set's confusion matrix diagram.

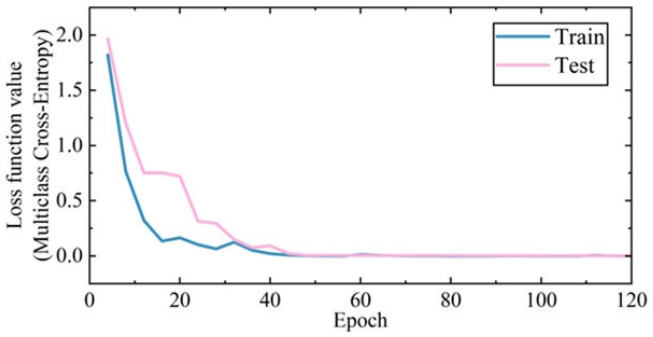

Fig. 9. Relationship between loss function value (multiclass cross-entropy) and epochs in the classification network.

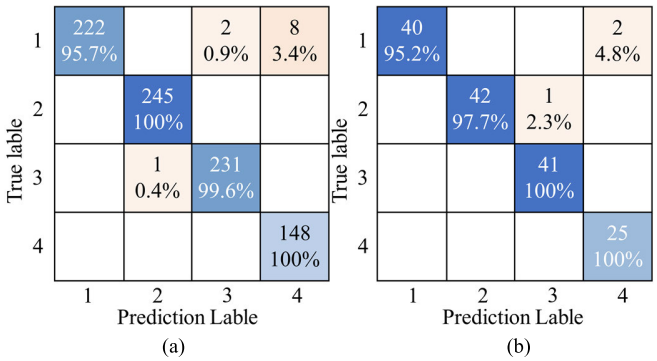

Fig. 10. Confusion matrix diagram of the localization network. (a) Training set's confusion matrix diagram. (b) Test set's confusion matrix diagram.

Fig. 9 shows the relationship between loss function value and epochs. The multiclass cross-entropy is used as the loss function. Multiclass cross-entropy is used to handle multiple classes, calculating the cross-entropy for each class and summing them up. The loss function measures the degree of difference between the predicted classification value and the true value. The smaller the loss, the closer the prediction is to the true label. The convergence of loss values reflects the efficiency of learning features of deep learning algorithms. The loss function is infinitely close to 0 and the change trend does not rebound. At this time, the network stops training and converges.

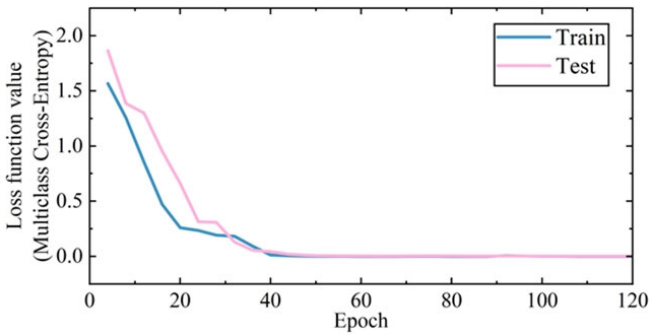

Fig. 11. Relationship between loss function value (multiclass cross-entropy) and epochs in the localization network.

Fig. 10 shows the confusion matrix diagram for judging the localization network of bleeding points. Fig. 10(a) is the final training set's confusion matrix diagram of the judgment results, and Fig. 10(b) is the test set's confusion matrix diagram of the judgment results. The abscissa represents the predicted label of the sample, where 1 represents top left, 2 represents top right, 3 represents bottom left, and 4 represents bottom right. The ordinate represents the true label of the sample. The accuracy of the training set is 98.7%. The accuracy on the test set is 98.0%. Fig. 11 shows the relationship between loss function value (multiclass cross-entropy) and epochs.

The above confusion matrixes show the feasibility of the method proposed in this article. To further verify the feasibility and practicability of the signal analysis method SEM and SSA-GA-BP network, the experimental verification of the brain phantom is carried out in Section V.

V. Experimental Verification

This section introduces the design, and test details of the experiment system. The experimental validation is a critical part. In this section, the details of establishing a phantom of the real human head are presented. The human head model consists of the skull, cerebrospinal fluid (CSF), white matter, gray matter, and blood in experiments. Antenna details around the model are also covered in this section. At the same time, the above algorithms are also verified in this experimental system.

A. Phantom Establishment of the Human Head

In this experimental system, a skull model is made based on real MRIs of real patients. The skull model is composed of two parts, one is a hollow skull and the other is a mandible. The main materials of this skull phantom are polyvinyl alcohol and calcium sulfate. The front of the skull phantom, the side of the skull phantom, the top of the skull phantom, and the interior of the skull phantom are shown in Fig. 12(a)–(d). This skull provides a container for filling the white matter and gray matter mimicking materials.

Fig. 13 is a skull model filled with mimicked brain tissue materials. At the same time, there are eight head phantoms with eight hemorrhagic sites at different locations established to obtain raw signals. The bleeding target is assumed by red

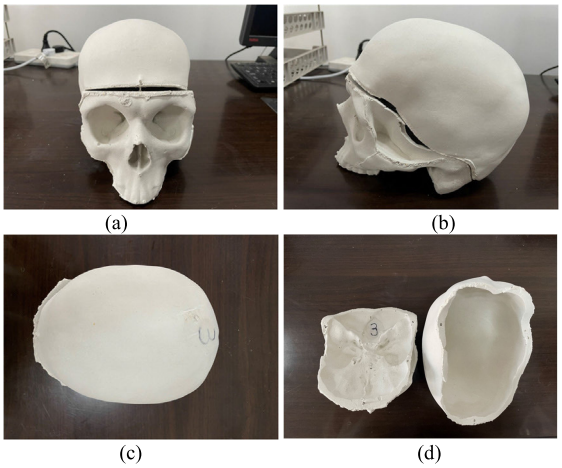

Fig. 12. Skull phantom used in this experiment. (a) Front of the skull phantom. (b) Side of the skull phantom. (c) Top of the skull phantom. (d) Interior of the skull phantom.

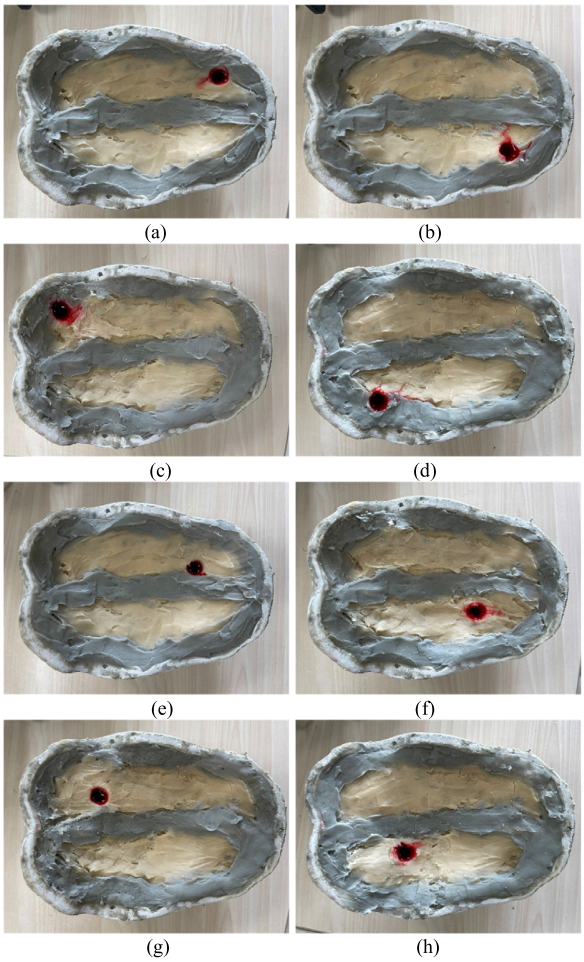

Fig. 13. Head phantom filled with tissue-mimicking materials. Eight hemorrhagic sites at different locations for experimental verification were replaced by red simulated fluid of 3 mL. (a) Top-right dura mater hemorrhage. (b) Bottom-right dura mater hemorrhage. (c) Top-left dural hemorrhage. (d) Bottom-left parenchymal hemorrhage. (e) Top-right parenchymal hemorrhage. (f) Bottom-right parenchymal hemorrhage. (g) Top-left parenchymal hemorrhage. (h) Bottom-left parenchymal hemorrhage.

simulated fluid with a volume of 3 mL. The composition of the red simulated blood material here is 1.5%–2% sodium alginate and 1% potassium chloride. Iron trioxide is used

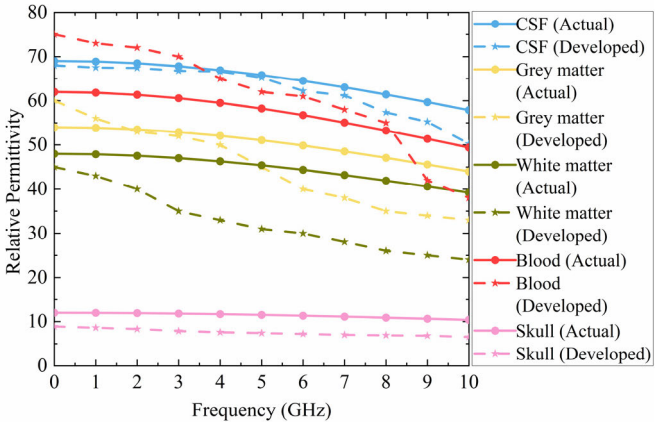

Fig. 14. Measured relative permittivity of the developed materials and the actual relative permittivity of real brain tissues.

as a coloring agent to make the color similar to that of blood. Fig. 13(a)–(d) are the top-right dura mater hemorrhage, the bottom-right dura mater hemorrhage, the top-left dura mater hemorrhage, and the bottom-left dura mater hemorrhage. Fig. 13(e)–(h) are the top-right parenchymal hemorrhage, bottom-right parenchymal hemorrhage, top-left parenchymal hemorrhage, and bottom-left parenchymal hemorrhage. In the experiment, red simulated blood with similar electrical properties to the real blood solution was used to fill in the simulated material. The bleeding target is with a size of 5 mm in radius. The use of simulated liquid filling is to mimic the real bleeding case that occurred in the human head.

The head model used in this experiment is a simplified model to validate the capability of the proposed signal-processing algorithm. Therefore, the skull, white matter, gray matter, and a small amount of CSF and blood are included. The electrical characteristics of the white matter, gray matter, CSF, and blood-mimicking materials inside the model are measured by the vector network analyzer in the 0–10-GHz frequency range at room temperature.

Fig. 14 shows the comparison between the measured electrical characteristics of the developed materials and the electrical characteristics of actual brain tissues. In this study, the scale of all the materials of the simulated brain tissue is adjusted to mimic the real brain tissue. So, the difference in the measured dielectric parameters between the developed material and the actual brain tissue is smaller than before [36], as shown in Fig. 14.

B. Antenna Design

The antenna used in this system is a "12-line Archimedes antenna." The working frequency range of the antenna is 0.8–10 GHz. The antenna size is 60 × 60 mm. The antenna feeding method adopts balun feeding to realize the impedance matching between the coaxial line and the radiator. The antenna used in this experiment is designed by electromagnetic simulation software, as shown in Fig. 15(a). Fig. 15(b) is the prototype of the antenna used in the experimental system. Fig. 16 is the photograph of the measurement setup for the used antenna. The reflection coefficient (S_{11}) obtained from the simulation and the measured reflection coefficient (S_{11}) of the used antenna are shown in Fig. 17. The frequency range of the used antenna in which the reflection coefficient is lower than −10 dB is 0.8–10 GHz.

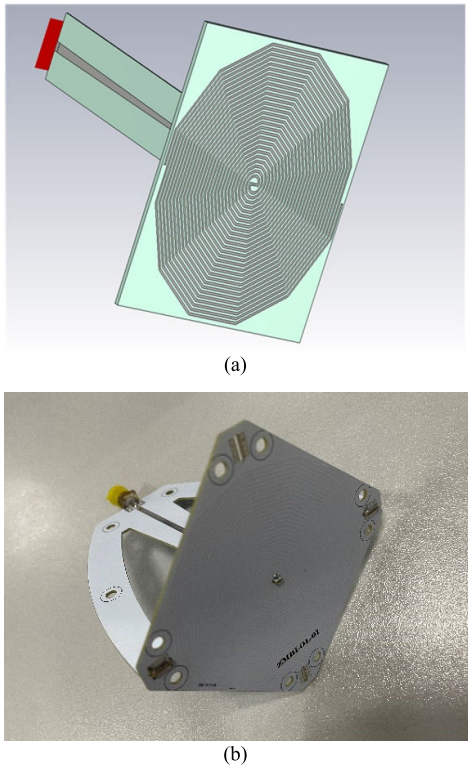

(a)

(b)

Fig. 15. Antenna model and antenna object. (a) Antenna model diagram in Electromagnetic simulation software. (b) Antenna's physical photograph.

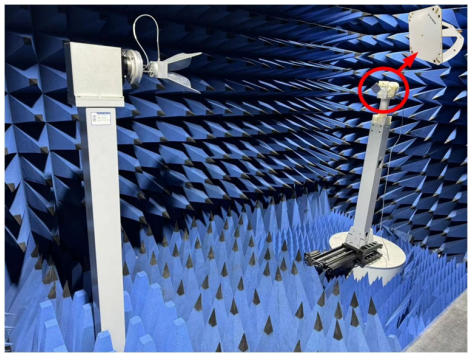

Fig. 16. Measurement setup of the used antenna.

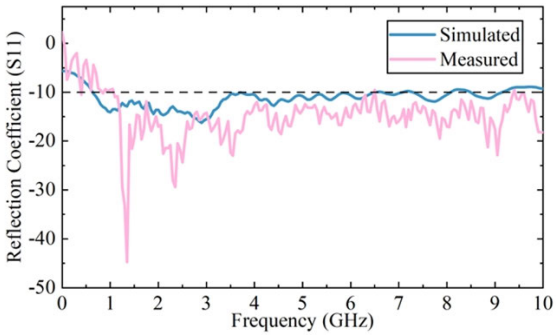

Fig. 17. Reflection coefficient (S_{11}) magnitude of the antenna in this experiment.

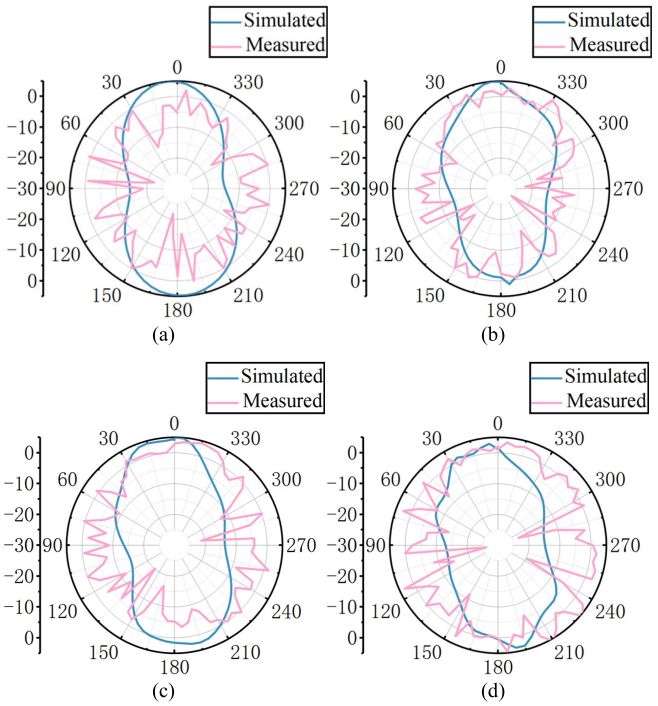

Fig. 18. Antenna radiation patterns of E-plane at different frequencies. (a) E-plane radiation pattern at 1 GHz. (b) E-plane radiation pattern at 3 GHz. (c) E-plane radiation pattern at 5 GHz. (d) E-plane radiation pattern at 7 GHz.

Fig. 18(a)–(d) is the simulated and measured far-field radiation patterns in the E-plane at 1, 3, 5, and 7 GHz. It can be observed in Fig. 18 that the simulated and measured far-field radiation patterns of the used antenna are similar over the whole frequency. The antenna has a wide half-power beamwidth (about 70°) at each measured frequency.

C. Experiment System Setup

The experiment system setup includes a vector network analyzer Agilent E5080B, a switch box, a laptop, an antenna array with eight antennas, and a head model. Fig. 19(a) shows the photograph of the experiment setup. The laptop is used to control the switch box. Four antennas are connected to port 1 of the vector network via the switching matrix, and the other four antennas are connected to port 2 of the vector network via the switching matrix. These eight antennas are evenly arranged around the head phantom. Fig. 19(b) shows the detailed diagram of the antenna arrangement and the location label of the bleeding target.

During the experiment, one signal was propagated in the head phantom through two antennas. A program in the laptop computer controls the RF switch box to switch the antenna. The obtained S_{21} results are displayed on the vector network analyzer. Eight groups of signals are stored by the laptop.

D. Experimental Verification

In this experiment system, the raw data are S_{21} which are detected in the range of 0.8–10 GHz. Fig. 20 shows four waveforms of S_{21}. $S_{21}(o5-2)$ is the S_{21} when antenna II emits a signal, antenna V receives the signal. $S_{21}(o5-3)$ is the S_{21} received by antenna V, when antenna III emits a signal.

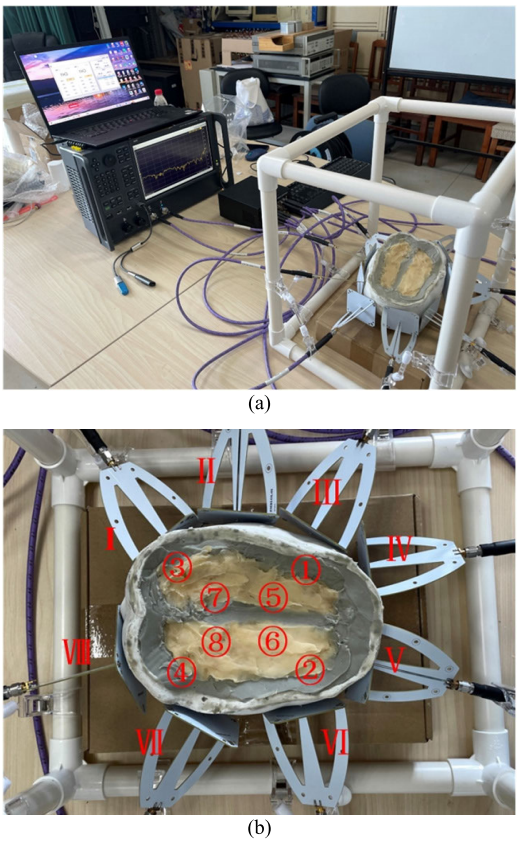

Fig. 19. Measurement setup. (a) Photograph of the measurement setup. (b) Photograph of detailed diagram of the antenna arrangement and the location label of the bleeding target.

Analogous to $S_{21}(o5-2)$ and $S_{21}(o5-3)$, $S_{21}(o5-7)$ and $S_{21}(o5-8)$ are the same. After getting all the S_{21}, these data are processed by inverse Fourier transform (IDFT) algorithm to obtain the time domain data. These time domain signals are set as the input data $y(t)$ in the Prony algorithm.

After the calculation of the Prony algorithm, the feature poles of different signals are obtained. Here, the feature poles are still used for two classifications. All the data are randomly divided into two groups. One group of data is used to train the neural network to identify the type of bleeding, and another set of data is for the second network to identify the direction of bleeding. Due to a lack of materials that mimic the dura mater of the brain, there are two labels for the type of bleeding: one refers to dural bleeding, and the other one refers to parenchymal bleeding. Eight positions of the bleeding point are shown in Fig. 19(b). Positions 1–4 are dural bleeding, and positions 5–8 are parenchymal bleeding. The orientation labels are divided into four categories: 1) 5 are top right; 2) 6 are bottom right; 3) 7 are top left; and 4) 8 are bottom left. The 136 feature poles are used in the network to determine the type of bleeding. The 116 feature poles are used for the training set, and 20 feature poles are used for the test set. The other 133 feature poles are used to judge the bleeding direction. The 114 feature poles are used for the training set, and 19 feature poles are used for the test set.

The above two sets of data are, respectively, input to two SSA-GA-BP networks which are shown in Fig. 21 for training.

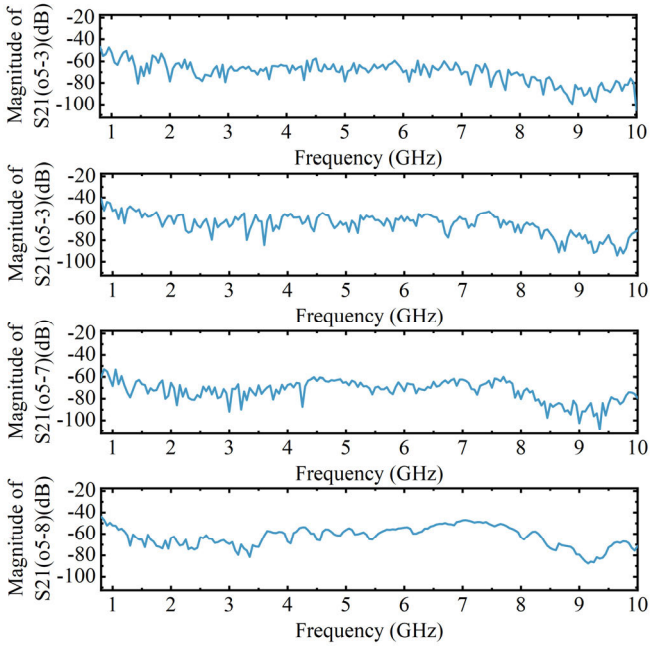

Fig. 20. S_{21} received by antenna V and emitted by antennas II, III, VII, and VIII, respectively, under the condition of simulating the bleeding point in position 1.

During the experimental verification, the SSA-GA-BP network is used because of the actual signal noise problem. The significance of extracting the poles of the original signals is that noise has an impact on experimental original signals. The SEM pole extraction is applicable for processing noise signals. The SSA is added in the experimental verification to optimize the number of nodes, and GA to optimize the weight and bias. As a result, the optimal network is given. In this way, SSA and GA are processed in parallel to form an overall optimization algorithm, which improves the accuracy when the number of training samples is small in the experiments.

Fig. 21(a) is the first neural network for judging the type of bleeding point. The number of nodes in the first hidden layer is 14, the number of nodes in the second hidden layer is 18, and the number of nodes in the output layer is 2. Fig. 21(b) is the second neural network for judging the direction of the bleeding point in the experimental verification phase. This neural network is a single hidden layer neural network with 16 nodes, and the number of nodes in the output layer is 4.

Fig. 22 shows the confusion matrix of the final training set and test set in the classification network. Fig. 22(a) is the final training set's confusion matrix of the classification results. Fig. 22(b) is the final test set's confusion matrix of the classification results. Fig. 23 shows the relationship between the multiclass cross-entropy and epochs during the training of the bleeding-type classification network. It can be seen in the figure that within the set epochs, the network converges. Fig. 24 shows the confusion matrix of the final training set and test set in the localization network. Fig. 24(a) is the training set's confusion matrix with the localization results. Fig. 24(b) is the test set's confusion matrix with the localization results. Fig. 25 shows the relationship between the

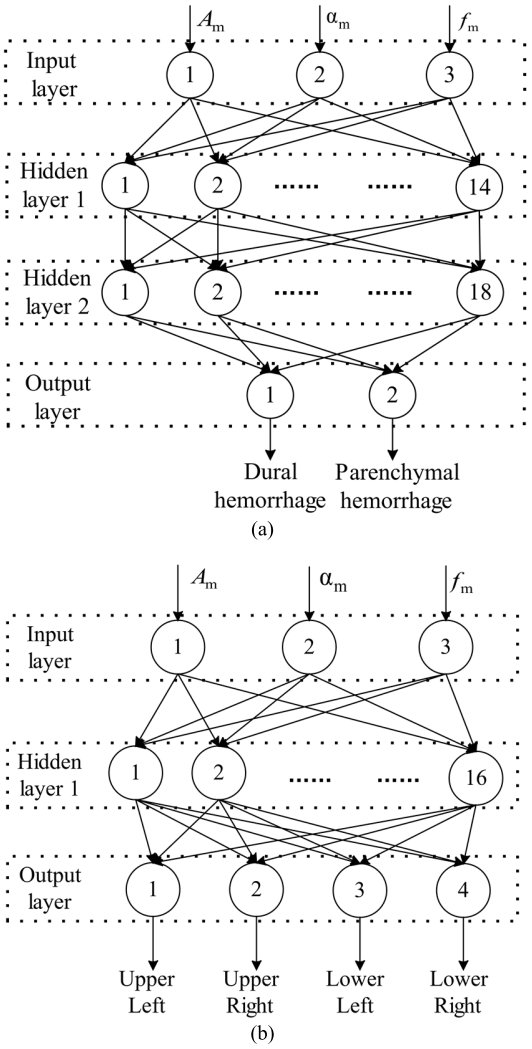

Fig. 21. Final network structure optimized by the genetic algorithm and SSA algorithm. (a) First neural network for judging the type of bleeding point. (b) Second neural network for judging the direction of the bleeding point.

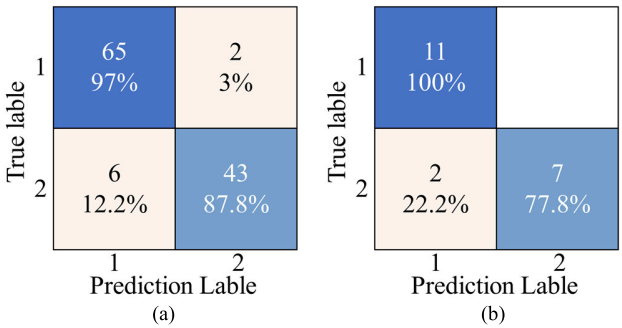

Fig. 22. Confusion matrix diagrams of classification neural network. (a) Training set's confusion matrix diagram. (b) Test set's confusion matrix diagram.

multiclass cross-entropy and epochs during the training of the bleeding localization network.

In this experiment, the final accuracy rate of the training set for classifying the type of bleeding point is 93.1%, and the final accuracy rate of the test set is 90%. The final accuracy rate of the training set for judging the location of

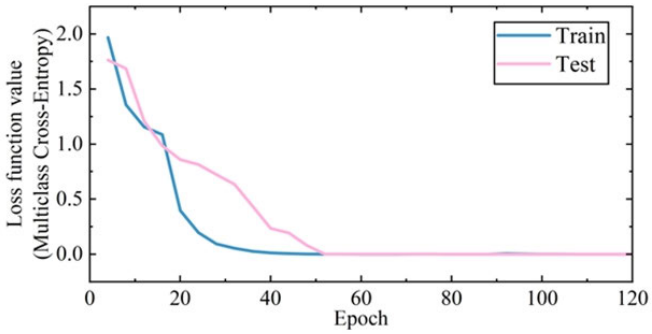

Fig. 23. Relationship between the loss function value (multiclass cross-entropy) and epochs in the classification network.

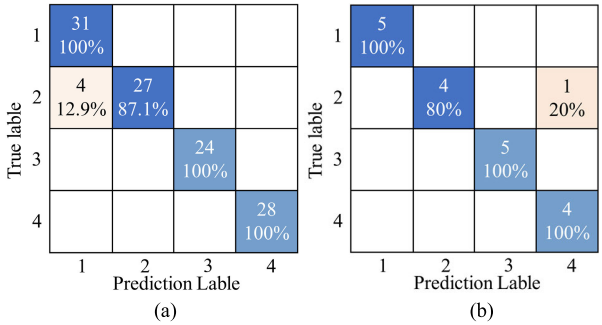

Fig. 24. Confusion matrix diagram of the localization neural network. (a) Training set's confusion matrix diagram. (b) Test set's confusion matrix diagram.

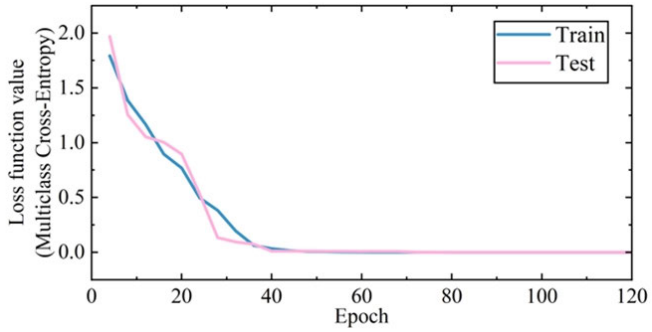

Fig. 25. Relationship between the loss function value (multiclass cross-entropy) and epochs in the localization network.

the bleeding point is 96.5%, and the final accuracy rate of the test set is 94.7%. Although there are some classification errors, the overall classification accuracy is good. The location of simulated bleeding targets in physical brain phantoms can be successfully detected and classified. The final results of the experiment prove that the detection algorithm proposed in this article is robust.

VI. Conclusion

Cerebral hemorrhage is a disease with a high fatality rate. The localization and classification of cerebral hemorrhage are judged directly by microwave signal, which saves precious life-saving time for patients. This study proposes a method for quickly determining the type and direction of the bleeding point. The simulation experiment and the designed microwave cerebral hemorrhage detection system are used to verify the feasibility of the Prony characteristic singularity signal processing algorithm combined with the SSA-GA-BP network. In the simulation, the test accuracy of classification and localization of the type of bleeding was 97.4% and 98.0%, respectively, which means the bleeding target with a radius of 3 mm can be located and classified successfully.

To validate the applicability of this method, experimental verification was conducted. The ability of the proposed method was demonstrated on a head phantom filled with developed materials of each brain tissue. In the experiment, the test accuracy of classification and localization of the bleeding type are 90% and 94.7%, respectively. The results show that the proposed method can successfully identify cerebral hemorrhage with a volume of 3 mL. After accurate computer timing, 20 s are taken for the processing procedure (including signal extraction, signal feature poles information extraction, and using the trained well network to get the final classification result).

The method proposed in this article still takes less time in the whole detecting procedure compared with the general medical instruments. All the results in this article show that the proposed method saved a lot of time for testing. In an emergency, it means more lives can be saved.

In this study, the original microwave signal data is not used to directly input the neural network for training. The feature pole information extracted by the signal processing algorithm in the early stage is the data input to the neural network. The reason why pole extraction is necessary can be divided into two categories. The first is the stability of the final results. The "end-to-end" mode is the original microwave signal directly input to the neural network. The neural network in this mode requires more parameters. This will cause more uncertainty. This type of judgment has more factors of interference, which will cause poor stability. While the input data is the processed signal rather than the original signal, it is more stable. The second is to use neural networks as an auxiliary tool for judgment. It means that signal processing is an important part of this study. The classification and localization do not depend entirely on the learning of neural networks.

In the future, different sizes of the hemorrhage point could be detected to help improve the applicability of this proposed method. More situations of the real human brain will be considered to improve the detection accuracy of the cerebral hemorrhage point.

References

[1] X. Ding et al., "Dipping pattern and 1-year stroke functional outcome in ischemic stroke or transient ischemic attack," *Clin. Experim. Hypertension*, vol. 45, no. 1, pp. 1–2, Dec. 2022.

[2] I. Bisio et al., "Variable-exponent Lebesgue-space inversion for brain stroke microwave imaging," *IEEE Trans. Microw. Theory Techn.*, vol. 68, no. 5, pp. 1882–1895, May 2020.

[3] A. Fedeli, A. Randazzo, A. Sciarrone, I. Bisio, F. Lavagetto, and M. Pastorino, "A microwave diagnostic technique for early-stage brain stroke characterization," in *Proc. 33rd Gen. Assem. Sci. Symp. Int. Union Radio Sci.*, Aug. 2020, pp. 1–3.

[4] I. Bisio et al., "A tomographic multistatic system for biomedical microwave sensing," in *Proc. 14th Eur. Conf. Antennas Propag. (EuCAP)*, Mar. 2020, pp. 1–4.

[5] M. Salimitorkamani, H. Odabasi, and G. Turan, "Wide-band metasurface antenna for microwave brain imaging systems," in *Proc. 34th Gen. Assem. Sci. Symp. Int. Union Radio Sci. (URSI GASS)*, Aug. 2021, pp. 1–4.

[6] A. Hossain and Md. A. Islam, "Design and optimization of an UWB monopole antenna with a two-branch feeding strip for brain stroke detection," in *Proc. 5th Int. Conf. Electr. Inf. Commun. Technol. (EICT)*, Dec. 2021, pp. 1–6.

[7] G. Zhu, A. Bialkowski, L. Guo, B. Mohammed, and A. Abbosh, "Stroke classification in simulated electromagnetic imaging using graph approaches," *IEEE J. Electromagn., RF Microw. Med. Biol.*, vol. 5, no. 1, pp. 46–53, Mar. 2021.

[8] I. Merunka, A. Massa, D. Vrba, O. Fiser, M. Salucci, and J. Vrba, "Microwave tomography system for methodical testing of human brain stroke detection approaches," *Int. J. Antennas Propag.*, vol. 2019, pp. 1–9, Mar. 2019.

[9] M. Hopfer, R. Planas, A. Hamidipour, T. Henriksson, and S. Semenov, "Electromagnetic tomography for detection, differentiation, and monitoring of brain stroke: A virtual data and human head phantom study," *IEEE Antennas Propag. Mag.*, vol. 59, no. 5, pp. 86–97, Oct. 2017.

[10] A. Randazzo et al., "An electrical impedance tomography system for brain stroke imaging based on a Lebesgue-space inversion procedure," *IEEE J. Electromagn., RF Microw. Med. Biol.*, vol. 5, no. 1, pp. 54–61, Mar. 2021.

[11] I. Bisio et al., "Brain stroke microwave imaging by means of a Newton-Conjugate-Gradient method in L_p Banach spaces," *IEEE Trans. Microw. Theory Techn.*, vol. 66, no. 8, pp. 3668–3682, Jul. 2018.

[12] D. O. Rodriguez-Duarte, J. A. T. Vasquez, R. Scapaticci, L. Crocco, and F. Vipiana, "Assessing a microwave imaging system for brain stroke monitoring via high fidelity numerical modelling," *IEEE J. Electromagn., RF Microw. Med. Biol.*, vol. 5, no. 3, pp. 238–245, Sep. 2021.

[13] D. O. Rodriguez-Duarte, J. A. T. Vasquez, R. Scapaticci, L. Crocco, and F. Vipiana, "Brick-shaped antenna module for microwave brain imaging systems," *IEEE Antennas Wireless Propag. Lett.*, vol. 19, no. 12, pp. 2057–2061, Dec. 2020.

[14] V. Mariano, J. A. T. Vasquez, M. R. Casu, and F. Vipiana, "Brain stroke classification via machine learning algorithms trained with a linearized scattering operator," *Diagnostics*, vol. 13, no. 1, p. 23, Dec. 2022.

[15] O. Karadima, P. Lu, and P. Kosmas, "Comparison of 2-D and 3-D DBIM-TwIST for brain stroke detection and differentiation," in *Proc. 15th Eur. Conf. Antennas Propag. (EuCAP)*, Mar. 2021, pp. 1–4.

[16] O. Karadima, E. Razzicchia, and P. Kosmas, "Image improvement through metamaterial technology for brain stroke detection," in *Proc. 14th Eur. Conf. Antennas Propag. (EuCAP)*, Mar. 2020, pp. 1–4.

[17] O. Karadima et al., "Experimental validation of microwave tomography with the DBIM-TwIST algorithm for brain stroke detection and classification," *Sensors*, vol. 20, no. 3, p. 840, Feb. 2020.

[18] T. Pokorny et al., "On the role of training data for SVM-based microwave brain stroke detection and classification," *Sensors*, vol. 23, no. 4, p. 2031, Feb. 2023.

[19] M. Salucci, A. Gelmini, J. Vrba, I. Merunka, G. Oliveri, and P. Rocca, "Instantaneous brain stroke classification and localization from real scattering data," *Microw. Opt. Technol. Lett.*, vol. 61, no. 3, pp. 805–808, Nov. 2018.

[20] P. M. Meaney, C. J. Fox, S. D. Geimer, and K. D. Paulsen, "Electrical characterization of glycerin: Water mixtures: Implications for use as a coupling medium in microwave tomography," *IEEE Trans. Microw. Theory Techn.*, vol. 65, no. 5, pp. 1471–1478, May 2017.

[21] K. S. Zubair et al., "Investigation of dielectric spectroscopy response in normal and cancerous biological tissues using S-parameter measurements," *J. Electromagn. Waves Appl.*, vol. 32, no. 8, pp. 956–971, Dec. 2017.

[22] E. Ricci, E. Cianca, T. Rossi, M. Diomedi, and P. Deshpande, "Performance evaluation of novel microwave imaging algorithms for stroke detection using an accurate 3D head model," *Wireless Pers. Commun.*, vol. 96, no. 3, pp. 3317–3331, Apr. 2017.

[23] J. Lu and D. V. Thiel, "Computational and visual electromagnetism using an integrated programming language for undergraduate engineering students," *IEEE Trans. Magn.*, vol. 36, no. 4, pp. 1000–1003, Jul. 2000.

[24] I. Saitoh and N. Takahashi, "Stability of symplectic finite-difference time-domain methods," *IEEE Trans. Magn.*, vol. 38, no. 2, pp. 665–668, Mar. 2002.

[25] P. Han, Z. Liu, Q. Li, M. Yu, and R. Zhao, "Development of realistic numerical brain model based on MRIs for microwave brain stroke detection," in *Proc. IEEE 15th Int. Conf. Electron. Meas. Instrum. (ICEMI)*, Oct. 2021, pp. 212–216.

[26] M. Van Blaricum and R. Mittra, "Problems and solutions associated with Prony's method for processing transient data," *IEEE Trans. Electromagn. Compat.*, vol. EMC-20, no. 1, pp. 174–182, Feb. 1978.

[27] C. E. Baum, E. J. Rothwell, K.-M. Chen, and D. P. Nyquist, "The singularity expansion method and its application to target identification," *Proc. IEEE*, vol. 79, no. 10, pp. 1481–1492, Oct. 1991.

[28] S. Licul and W. A. Davis, "Unified frequency and time-domain antenna modeling and characterization," *IEEE Trans. Antennas Propag.*, vol. 53, no. 9, pp. 2882–2888, Sep. 2005.

[29] Y. Huo, R. Bansal, and Q. Zhu, "Breast tumor characterization via complex natural resonances," in *IEEE MTT-S Int. Microw. Symp. Dig.*, Jun. 2003, pp. 387–390.

[30] Y. Huo, R. Bansal, and Q. Zhu, "Modeling of noninvasive microwave characterization of breast tumors," *IEEE Trans. Biomed. Eng.*, vol. 51, no. 7, pp. 1089–1094, Jul. 2004.

[31] X. Zhang, K. Zhang, M. Jiang, and L. Yang, "Research on the classification of lymphoma pathological images based on deep residual neural network," *Technol. Health Care*, vol. 29, pp. 335–344, Mar. 2021.

[32] M. Liu, W. Guan, J. Yan, and H. Hu, "Correlation identification in multimodal Weibo via back propagation neural network with genetic algorithm," *J. Vis. Commun. Image Represent.*, vol. 60, pp. 312–318, Apr. 2019.

[33] D. Jia, C. Zhang, and D. Lv, "Evaluation of road condition based on BA-BP algorithm," *J. Intell. Fuzzy Syst.*, vol. 40, no. 1, pp. 331–348, Jan. 2021.

[34] Y. Yang, G. Wang, and Y. Yang, "Parameters optimization of polygonal fuzzy neural networks based on GA-BP hybrid algorithm," *Int. J. Mach. Learn. Cybern.*, vol. 5, no. 5, pp. 815–822, Jan. 2014.

[35] Y. Fu, Y. Liu, and Y. Yang, "Multi-sensor GA-BP algorithm based gearbox fault diagnosis," *Appl. Sci.*, vol. 12, no. 6, p. 3106, Mar. 2022.

[36] Q. Li et al., "A portable microwave intracranial hemorrhage imaging system based on PSO-MCKD-CEEMDAN method," *IEEE Trans. Microw. Theory Techn.*, vol. 71, no. 2, pp. 773–783, Feb. 2023.

Qinwei Li (Member, IEEE) received the B.S. and M.S. degrees in electronic science and technology and the Ph.D. degree from Tianjin University, Tianjin, China, in 2012, 2015, and 2019, respectively.

She is currently a Teacher with the College of Electronic Information and Automation, Civil Aviation University of China, Tianjin. Her current research interests include imaging algorithms, medical imaging, and signal processing.

Lunxiao Wang was born in Handan, Hebei, China, in 1999. She is currently pursuing the master's degree in electronic information and automation with the Civil Aviation University of China, Tianjin, China.

She is currently involved in research on microwave stroke imaging systems led by Qinwei Li. Her current research interests include 3-D modeling of the brain and microwave imaging systems for stroke.

Xiaoguang Lu (Member, IEEE) received the M.S. and Ph.D. degrees from the Civil Aviation University of China, Tianjin, China, in 2008 and 2014, respectively.

He is currently an Associate Professor with the College of Electronic Information and Automation, Civil Aviation University of China. His current research interests include radar signal processing, image processing and recognition, and monitor data processing.

Dequan Ding was born in Zhengzhou, Henan, China, in 2000. He is currently pursuing the master's degree with the Civil Aviation University of China, Tianjin, China.

He is currently involved in the study of microwave stroke imaging systems led by Qinwei Li. His current research interests include the design and optimization of ultra wide band (UWB) antennas.

Yang Zhao (Member, IEEE) received the B.S. degree in communication engineering from Hainan University, Haikou, China, in 2010, and the M.S. degree in information and communication engineering and the Ph.D. degree in electronic science and technology from Tianjin University, Tianjin, China, in 2012 and 2015, respectively.

From 2017 to 2018, she was a Visiting Scholar with Yale University, New Haven, CT, USA. Since 2018, she has been a Lecturer with the Communication Engineering Department, Civil Aviation University of China, Tianjin. Her research interests include the Internet of Things, RFID, wireless indoor localization, image processing, and pattern recognition.

Jianwei Wang (Member, IEEE) received the M.S. and Ph.D. degrees in electronic science and technology from Beihang University, Beijing, China, in 2017 and 2021, respectively.

He is currently an Associate Professor with the College of Electronic Information and Automation, Civil Aviation University of China, Tianjin, China. His research interests include the design of near-field probes, measurement/instrumentation of near-field measurements, and electromagnetic interference (EMI) source reconstruction.

Xinze Li was born in Yingkou City, China.

He was a Chemical Technology Engineer at the Biomaterials Technology Center of Yingkou Jucheng Teaching and Development Company Ltd. He has been serving as the Technical Director at the Biomaterials Technology Center, Yingkou Jucheng Teaching and Development Company Ltd., Huludao, China, since September 2012.

Hang Wu born in Chengdu, Sichuan, China, in 1991. He received the bachelor's degree from the School of Machinery, Tianjin University, Tianjin, China, in 2010, and the Ph.D. degree from the Academy of Military Medical Sciences, Tianjin, in 2017.

His current research direction is medical artificial intelligence and robotics.

Guang Zhang received the Ph.D. degree in biomedical engineering from the Academy of Military Medical Sciences, Beijing, China, in 2013.

His research interests include the integration of artificial intelligence for medical equipment and physiological signal processing.

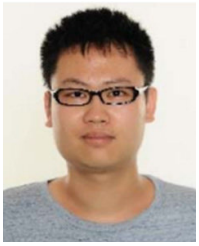

Ming Yu received the Ph.D. degree in biomedical engineering from the Academy of Military Medical Sciences, Beijing, China, in 2017.

He is currently an Engineer with the Medical Support Technology Research Department, Systems Engineering Institute, Academy of Military Science, Tianjin, China. He is mainly engaged in the research and development of physiological signal processing and machine learning.

Ping Han received the M.S. and Ph.D. degrees from Tianjin University, Tianjin, China, in 1989 and 2004, respectively.

She is currently a Professor with the College of Electronic Information and Automation, Civil Aviation University of China, Tianjin. Her current research interests include image processing and pattern recognition, synthetic aperture radar (SAR), and polarimetric synthetic aperture radar (PolSAR) image interpretation.